July 3, 2023

Submitted to Chem Eng J R2

Highly efficient and photostable conversion of bicarbonate to acetate by a pyrrolic nitrogen enriched Ag_3PO_4/g-C_3N_4 photocathode with an intermediate band level in photo-assisted microbial electrosynthesis systems

Weifeng Kong[1], Qiang Wang[2], Liping Huang[1,*], Xie Quan[1], Gianluca Li Puma[3,*]

1. Key Laboratory of Industrial Ecology and Environmental Engineering, Ministry of Education (MOE), School of Environmental Science and Technology, Dalian University of Technology, Dalian 116024, China

College of Chemistry, Dalian University of Technology, Dalian 116024, China

2. Jiangxi Academy of Eco-Environmental Sciences and Planning, Nanchang, 330000, China

3. Environmental Nanocatalysis & Photoreaction Engineering, Department of Chemical Engineering, Loughborough University, Loughborough, LE11 3TU, United Kingdom

lipinghuang@dlut.edu.cn (Huang L.)

g.lipuma@lboro.ac.uk (G. Li-Puma)

Declarations of interest: none

Abstract

A highly efficient and photostable acetate production from bicarbonate (HCO_3^-) reduction is demonstrated in a photo-assisted microbial electrosynthesis system (MES) using a pyrrolic nitrogen enriched Ag_3PO_4/g-C_3N_4 photocathode. Urea-treatment of the Ag_3PO_4/g-C_3N_4 photocathode synergistically improved the MES performance by up to 1.8 folds under visible light illumination, achieving acetate production of 9.6 mM/d with coulombic efficiency of 95%, negligible catalyst leaching, and solar-to-acetate efficiency of 1.15% over 12 days continuous operation. The photocorrosion of Ag_3PO_4 was efficiently inhibited by a two-step charge transfer process mediated by an intermediate band level introduced by oxygen-vacancies in the Ag_3PO_4 structure, which also facilitated light absorption and charge transfer through a Z-scheme mechanism, whereas the increased pyrrole N in the g-C_3N_4 provided supplementary active sites for direct and indirect (via H_2) electron transfer to *Serratia marcescens* electrotroph. This study demonstrates the ingenious use of photocatalytic heterojunctions for achieving step-changes in the MES performance.

Keywords: microbial electrosynthesis; photo-assisted; intermediate band; photocorrosion; pyrrolic nitrogen

1 Introduction

Photo-assisted microbial electrosynthesis system (MES) is a promising platform to realize the energy-intensive reduction reaction of inorganic carbon to value-added chemicals (e.g., acetate), which contributes to accomplish the goal of a circular energy economy with sustainable carbon neutrality [1-4]. Recently, it has been demonstrated that a one-order of magnitude change in the efficiency of chemicals production can be realized using photo-assisted MES, incorporating photocathodes combining electrotrophs with different photocatalytic semiconductors such as $WO_3/MoO_3/g\text{-}C_3N_4$ [2], Si nanowires/TiO_2/Ni [3], $CuO/g\text{-}C_3N_4$ [5], $MnFe_2O_4/g\text{-}C_3N_4$ [6] and $CuO/g\text{-}C_3N_4$/rGO [7]. Among these prototypes of such photocathodes for efficient acetate production, $Ag_3PO_4/g\text{-}C_3N_4$ has showed wide promising application for achieving high power for inorganic carbon reduction [8] due to efficient electron–hole pairs generation and separation based on its suitable redox potential and intrinsic Z-scheme charge transfer mechanism. In this way, the photogenerated electrons of Ag_3PO_4 are excited from the valence band (VB) to its conduction band (CB) and then recombined with the photoinduced holes from $g\text{-}C_3N_4$ at the interface of the heterojunction, eventually accumulating reductive electrons on the CB of $g\text{-}C_3N_4$ to generate an excess of reducing equivalents for acetate production [8-10]. However, the $Ag_3PO_4/g\text{-}C_3N_4$ suffers severely from poor photostability and operational fluctuation under illumination due to photocorrosion of Ag^+. The photoreduction of Ag^+ to metallic Ag is caused by the redundant accumulation of electrons on the CB of Ag_3PO_4 due to the narrower band gap in comparison to $g\text{-}C_3N_4$, since the recombination of electron-hole charges in the

Z-scheme charge transfer mechanism is controlled by the smaller fraction of photoinduced holes in the VB of g-C_3N_4 [8,11,12]. Despite the fact that photoetching of a Ag_3PO_4/g-C_3N_4 photocathode can be mitigated by the photoreduction of the in-situ produced H_2O_2 [8], this process inevitably also consumes a fraction of photogenerated electrons, and thus negatively influenced the performance of the photo-assisted MES. The occurrence of photocorrosion in such case and in many other irradiated semiconductors, not only limited to the well-known CdS, CuO_2 and AgCl, has advocated the need of developing new ways of stabilizing and improving the photocatalytic activities of these materials [11].

In conventional photocatalysis processes introducing an isolated intermediate band (IB) by creating sufficient vacancies [13,14] or doping ions [15,16] within the band gap of a photocatalyst, has been recently reported to switch the charge transfer pathway from a one-step optical transition to a two-step transition, with the first from the VB to the IB and the second from the IB to the CB of the photocatalyst, leading to either higher hydrogen production or antibiotics degradation [13-16]. Such a strategic approach simultaneously decelerated the charge transfer and prolonged the lifetime of charge carriers, ultimately alleviating the redundant accumulation of electrons on the CB of the semiconductor and reducing the recombination of photoinduced electron-hole pairs [13-16]. Therefore, this two-step transition mediated by IB originating from sufficient vacancies, might also be utilized in photo-assisted MES for effectively inhibiting the photocorrosion of the semiconductors, favoring the production of hydrogen and higher rates of acetate production via the Wood-Ljungdahl pathway [1-

4].

The extraction of oxygen from the metal oxide lattice by using a urea reducing atmosphere is an effective approach for the creation of oxygen vacancies within the semiconductor, and above a certain concentration threshold a new energy level with delocalized properties can create an actual intermediate band [13,16,17]. The visible-light responsive photocatalyst Ag_3PO_4 inherently possesses higher crystallinity and a higher concentration of lattice oxygen [11,18] for the introduction of adequate oxygen vacancies to form IB in comparison to other photocatalyst, such as $MnFe_2O_4$. It is thus expected that urea treatment of Ag_3PO_4 with sufficient oxygen vacancies can mitigate its photocorrosion by the IB mediated two-step optical transition, reaching stable and high-efficient inorganic carbon reduction to acetate production in the photo-assisted MES. Additionally, hydrothermal treatment of g-C_3N_4 in the presence of urea, can alter the N configuration of g-C_3N_4 improving the pyrrolic N content [6,19]. This occurs because of the replacement of the carbon atoms on the edges of the graphitic structure with N element forming pyrrolic N, compared to the graphitic N and pyridinic N [19-21]. Importantly, pyrrolic N possesses the strongest affinity and the lowest adsorption energy to the central functional porphyrin iron of the outer membrane *c*-type cytochromes among these three N configurations, and thus enables faster extracellular electron transfer process and stronger interactions between electrotrophs and catalysts [20,21]. Notably, pyrrolic N can also function as the active site to rapidly enhance the interfacial catalytic reaction and promote the photogenerated electrons transfer for boosting hydrogen production in conventional photocatalytic processes [22,23]. These

111 three aspects associated with the treatment of Ag_3PO_4/g-C_3N_4 with urea, might in
112 concert produce a significant MES performance improvement over previous studies,
113 such as those describing the inhibition of Ag_3PO_4/g-C_3N_4 photoetching by in-situ
114 production of H_2O_2 [8] which consumes photoinduced electrons.

115 Herein, a highly photostable pyrrolic nitrogen enriched Ag_3PO_4/g-C_3N_4
116 photocathode with an IB and superior charge transfer ability prepared by urea treatment
117 was demonstrated in a photo-assisted MES to achieve significantly higher acetate
118 production from the reduction of bicarbonate (HCO_3^-) using the nonphotosynthetic
119 *Serratia marcescens* Q1 electrotroph [2]. Based on the collective results obtained by
120 UV-vis diffuse reflection spectroscopy (UV-vis DRS), photoluminescence (PL), Mott-
121 Schottky curves, X-ray photoelectron spectrometry (XPS), electron spin resonance
122 (ESR) and other characterization methods, a charge transfer mechanism with a two-step
123 optical transition mediated by the oxygen-vacancy induced IB, inhibiting photoetching
124 and with pyrrolic N acting as an effective electron active site and transfer platform was
125 proposed, to account for the improved inorganic carbon reduction in the MES with the
126 urea-treated Ag_3PO_4/g-C_3N_4 photocathode. This study demonstrates a new promising
127 way for synthesizing highly efficient semiconductor heterojunctions with anti-
128 photocorrosion properties and preferable and rational charge transfer, which can
129 achieve highly-efficient and stable production of acetate from the reduction of inorganic
130 carbon in photo-assisted MES.

131

132 **2 Materials and methods**

133 *2.1 Preparation of photocathodes*

134 The urea-treated Ag_3PO_4/g-C_3N_4 was synthesized as Fig. S1. The urea-untreated
135 g-C_3N_4 was prepared in a typical procedure [6], where 10 g melamine was heated to
136 550 ℃ for 4 h with a heating rate of 3 ℃/min and then cooled to room temperature to
137 fabricate, while the urea-treated g-C_3N_4 was synthesized by the mixture of urea and
138 melamine as the same procedures. The urea-untreated g-C_3N_4 was then dissolved in 60
139 mL deionized water with 45 min ultrasonication, after which 0.936 g $AgNO_3$ was added
140 in the solution and continuously ultrasonicated for 20 min. 0.714 g $Na_2HPO_4 \cdot 12H_2O$
141 and different amounts of urea (0, 0.098, 0.197, 0.295, 0.394 g) were then dosed in the
142 above mixture with 1 h magnetic stirring under 60 °C. Thereafter, the above mixture
143 was sealed in a Teflon-lined autoclave and heated at 200 ℃ for 12 h to obtain the desired
144 urea-treatment Ag_3PO_4/g-C_3N_4.

145 The urea-treated Ag_3PO_4 was fabricated using the same processes without the
146 addition of g-C_3N_4. The urea-untreated controls were similarly synthesized with the
147 same procedures of urea-treated samples but without the urea addition.

148 The preparation of urea-treated or urea-untreated Ag_3PO_4/g-C_3N_4 photocathodes
149 using graphite felts (2.0 cm × 2.0 cm × 0.25 cm, Sanye Co., Beijing, China) as substrates
150 were based on an impregnation method [8], as described in Supporting Information (SI).

151

152 *2.2 Reactor construction, electrotroph inoculation and operation*

153 Two-chamber reactor with each internal volume of 28 mL (26 mL effective
154 working volume) was separated by a cation exchange membrane (CMI-7000

155 Membranes International, Glen Rock, NJ). The urea-treated Ag_3PO_4/g-C_3N_4 was used
156 as cathode and a saturated calomel electrode (SCE) as the reference electrode, while a
157 carbon rod served as the anode. All potentials were reported versus standard hydrogen
158 electrode (SHE) unless stated otherwise. The anode chamber was inoculated from
159 microbial fuel cells and fed with nutrient solution [24], while a non-photosynthetic
160 electrotrophic *S. marcescens* Q1 with the ability to reduce inorganic carbon for acetate
161 production [2,25], was inoculated to the cathode chamber at an appropriate OD_{600} of
162 0.35, as previously reported [2]. The non-photosynthetic *S. marcescens* (GenBank
163 MT982676.1) has been reported to produce acetate, formate or alcohols from inorganic
164 carbon [2,25-29]. The catholyte contained mineral (0.6 mL/L), vitamins (0.6 mL/L),
165 NH_4Cl (2.1 mM), $NaHCO_3$ (23.8 mM), and KH_2PO_4 (0.09 mM) with a pH of 5.8 [2].
166 More acidic pHs can positively impact the (photo)electrochemical production of H_2
167 [30], which is used *in-situ* by *S. marcescens* for inorganic carbon reduction to acetate
168 or to other minor organic substances [2,28,29]. Conversely, in terms of pH-dependent
169 inorganic carbon species, a neutral pH exhibits the equilibrium HCO_3^- (92%), CO_2 (6%)
170 and CO_3^{2-} (2%), compared to the equivalent HCO_3^- (50%) and CO_2 (50%) at an acidic
171 pH 5.8 [31]. In previous studies, as a compromise, a pH of 5.8 and $NaHCO_3$
172 concentration in the range 29.8 – 47.6 mM was advocated for acetate production from
173 inorganic carbon reduction [32,33]. In this study, a pH of 5.8 and $NaHCO_3$ of 23.8 mM
174 were chosen throughout the experiments. Before adding to the MES reactor, the
175 catholyte was bubbled with N_2 gas for 15 min to obtain an anaerobic environment [34].
176 All the reactors were applied with a cathode potential of –1.1 V vs. SHE and kept at 25

± 3 ℃ [2]. The selection of this cathode potential, instead of less negative potentials (e.g., –0.6 V), yields sufficiently higher circuital currents that favors the production of adequate reduction equivalent (H_2) utilized in-situ by *S. marcescens* Q1 with inorganic carbon for the production of acetate through Wood–Ljungdahl pathway, as previously illustrated [2], and is similar to many other pure MESs or photo-assisted MESs [3,35-37]. A 100 W iodine tungsten lamp with a light intensity of 23.3 mW/cm^2 was employed as light source [2,24]. The stability of the urea-treated Ag_3PO_4/g-C_3N_4 photocathode was examined over 12 days continuous operation, with periodical supply of $NaHCO_3$ to guarantee adequate inorganic carbon for efficient acetate production. All operations were conducted in triplicate and all the data were collected after the first operational cycle [2,8].

2.3 Characterizations

The surface structure and composition analyses were studied by X-ray diffraction (XRD, Shimadzu, Japan) using Cu Kα radiation, XPS (ESCALAB250, Thermo, USA), transmission electron microscopy (TEM, Tecnai G2 F30 S-Twin, FEI, USA) and scanning electron microscopy (SEM, Nova NanoSEM 450, FEI company, USA) equipped with an energy dispersive X-ray spectroscopy (EDS). It is worthwhile to note that the photocathodes after certain periodical operation were removed from the reactors and routinely dried in inert Ar_2 atmosphere to exclude the likely occurrence of photocorrosion by any active species. The Brunauer–Emmett–Teller (BET) specific surface areas were characterized by Quadrasor-SI (Quantachrome, USA). The optical

properties were characterized by UV–vis DRS (Lambda 750S, Perkin-Elmer, USA), PL (F-4500, Hitachi, Japan) and transient photocurrent response (BioLogic, VSP, France). ESR analysis was conducted on a Bruker A200 (Karlsruhe, Germany).

Differential pulse voltammetry (DPV) was recorded with a scan rate of 0.1 mV/s at an amplitude of 50 mV and a pulse period of 1 s. The scan rate of 0.1 mV/s instead of a rapid scan rate (e.g., 1.0 mV/s) has been proven to guarantee a sufficiently long time for the system to reach steady conditions [38,39]. Electrochemical impedance spectroscopy (EIS) was conducted with an amplitude of 5 mV in a frequency range from 0.01 ~ 100 kHz, where Nyquist plots of the impedance spectra was obtained from Zsimpwin software. All the electrochemical measurements were conducted by a typical three-electrode cell with a working electrode, a reference SCE (+0.241 V versus SHE), and a Pt counter electrode. The project surface area (2.0 cm × 2.0 cm, 4.0 cm^2) of this Pt counter electrode, appreciably larger than the carbon rod (diameter: 1.0 cm, 0.8 cm^2), reasonably exhibited less polarization than the carbon rod anode, and thus adapted well for the analysis of the working cathode electrode [39,40].

2.4 Analytical methods

A gas chromatograph (GC7900, Tianmei, China) was used to analyze residual hydrogen in the headspace of cathode chamber and acetate production in the catholyte. The residual inorganic carbon was measured by the national standard method (DZ/T 0064.49-93), while the leached catalyst was analyzed by atomic absorption spectroscopy (AAnalyst 700, PerkinElmer). The coulombic efficiency for acetate

production ($CE_{acetate}$), the solar-to-acetate efficiency (ξ) and the overall energy efficiency (η) were calculated as follows [3,6,41]:

$$CE_{\text{acetate}} = \frac{8 \times n_a \times \text{F}}{\int_0^t Idt} \times 100\%$$

$$\xi = \frac{\Delta\text{G} \times n_a}{E_\text{p} \times A \times t} \times 100\%$$

$$\eta = \frac{\Delta\text{G} \times n_a}{E_\text{p} \times A \times t + E_\text{ap} \times I \times t} \times 100\%$$

where n_a (mol) is the mole of acetate, I (A) is the current, ΔG (369.41×10^3 J/mol) is the Gibbs free energy of acetate, F (96485 C/mole electron) is the Faraday constant, E_p (W/cm^2) is the light intensity, t (s) is the operation time, A (cm^2) is the projected area of cathode, and E_{ap} (V) is the external applied voltage of the MES.

Statistical variation of the data was analyzed by one-way ANOVA in SPSS 19.0, and all of the data indicated statistically significant of a p value < 0.05.

3 Results and discussion

3.1 Characterization of photocatalysts

All the characteristic XRD peaks of Ag_3PO_4 were assigned to the cubic phase of Ag_3PO_4 (JCPDS No.06–0505) [8,9], while the peaks of 12.6° (100) and 27.4° (002) were well indexed to g-C_3N_4 (Fig. 1A and Fig. S2A) [42-44]. The XRD profiles of Ag_3PO_4/g-C_3N_4 overlapped all the characteristic peaks of the two single semiconductors, confirming the successful combination of Ag_3PO_4 and g-C_3N_4 in the heterojunction. The peaks at about 25.5° in all the cathode XRD results were ascribed to the graphite felt, indicating the successful combination of the graphite felt substrate with the photocatalysts [8,45]. Similar diffraction peaks without other impurity phases

243 of the photocatalysts with and without urea treatment suggested urea treatment did not
244 affect the basic crystal structure of the semiconductors. Moreover, no characteristic
245 peak related to metallic Ag was observed in all the Ag_3PO_4 and Ag_3PO_4/g-C_3N_4
246 photocatalysts (Fig. 1A and Fig. S2A), indicating the absence of photocorrosion for the
247 fresh photocatalysts.

248 **Here Fig. 1**

249 The Ag_3PO_4/g-C_3N_4 XPS spectra (Fig. 1B and C, Fig. S2B−D) contained the
250 elements of C, N, O, P and Ag, confirming that Ag_3PO_4 was successfully loaded on the
251 surface of g-C_3N_4. Compared to the peak positions of g-C_3N_4 or Ag_3PO_4, regardless of
252 urea treatment, it is noteworthy that the binding energies of C 1s and N 1s had slight
253 negative shifts, while O 1s, P 2p and Ag 3d shifted towards higher binding energies.
254 The opposite binding energy shifts of different elements in the heterojunction suggested
255 the migration of photogenerated electrons from Ag_3PO_4 to g-C_3N_4 following a Z-
256 scheme mechanism [46]. Specially, the high resolution XPS spectra of N 1s (Fig. 1B)
257 were deconvoluted with three peaks at about 399 eV (pyridinic N), 400 eV (pyrrolic N)
258 and 401 eV (graphitic N) [20,21], where variation of N configurations were observed
259 with obvious increase of pyrrolic N contents due to urea treatment (Table S1) [19], in
260 both the single g-C_3N_4 phase (43.6% vs. 30.2%) and in the Ag_3PO_4/g-C_3N_4
261 heterojunction (42.7% vs. 29.6%). Moreover, the oxygen species at the oxygen vacancy
262 sites with an appreciably broader peak centered at about 531 eV [13,14] was detected
263 in the O 1s spectra (Fig. 1C) of the urea-treated Ag_3PO_4/g-C_3N_4 (52.1%) and in single
264 Ag_3PO_4 phase (51.7%), compared to the untreated controls (Ag_3PO_4/g-C_3N_4: 22.2%;

265 Ag_3PO_4: 21.3%; Table S1). Combining with the higher intensities of characteristic
266 oxygen vacancy signals centered at g = 2.002 in the ESR spectra [13] of both Ag_3PO_4/g-
267 C_3N_4 and single-phase Ag_3PO_4 photocatalysts after urea treatment (Fig. 1D), all the
268 results suggested that abundant oxygen vacancies were introduced by urea treatment to
269 provide the possibility of forming an intermediate band in the Ag_3PO_4.

270 All the N_2 adsorption-desorption isotherms of Ag_3PO_4/g-C_3N_4 (Fig. S2F)
271 presented type IV isotherms with hysteresis loops, which reflected the mesoporous
272 structures of the heterojunctions. The higher surface area of the urea-treated Ag_3PO_4/g-
273 C_3N_4 (65.7 m^2/g), compared to the untreated control (48.2 m^2/g), could provide more
274 active reaction sites for the photo-assisted process [6,15,43].

275 Similar morphological characteristics in the SEM (Fig. 2A−C and Fig. S3) and
276 TEM (Fig. S4) images of Ag_3PO_4/g-C_3N_4 before and after urea treatment, where the
277 irregular polyhedral Ag_3PO_4 [9,10] was closely and evenly anchored on the g-C_3N_4
278 nanosheets without obvious agglomerations, suggested that urea treatment did not
279 distinctly influence the morphology of photocatalysts. The lattice fringe spacing of
280 0.265 nm in the heterojunction (Fig. S4B and D) was assigned to Ag_3PO_4 (210) crystal
281 plane, exactly similar to that exhibited in the pure Ag_3PO_4 (Fig. S4F) [8-10]. The
282 homogeneously distributed elemental mapping of Ag, P, O, C and N (Fig. 2D−H) on
283 the surface of the photocathode demonstrated that Ag_3PO_4 nanoparticles were
284 uniformly loaded on the surface of g-C_3N_4 nanosheets. These along with the
285 coexistence of all the elements signals in the EDS spectra of the Ag_3PO_4/g-C_3N_4
286 heterojunction (Fig. 2I), collectively verified the successful preparation of target

287 photocatalysts again. The dense and uniform attachment of *S. marcescens* on both
288 Ag_3PO_4/g-C_3N_4 (Fig. 2C) and g-C_3N_4 (Fig. S3C) bio-photocathodes, compared to the
289 Ag_3PO_4 control (Fig. S3F), reflected the excellent biocompatibility of the g-C_3N_4 for
290 keeping the electrotroph in high viability, corresponding to the higher EDS signals of
291 Na, P and K (Fig. S5).

292 **Here Fig. 2**

293 *3.2 Band-gaps, charge separation and photoactivity*

294 Combined UV-vis DRS, PL and transient photocurrent response analyses were
295 performed to evaluate the optical absorption, and charge generation and separation
296 properties of the photocatalysts. The absorption edge of the urea-treated Ag_3PO_4/g-
297 C_3N_4 heterojunction (579 nm) was obviously higher than in the controls: either the
298 untreated Ag_3PO_4/g-C_3N_4 (550 nm) or the urea-treated single phase photocatalysts
299 (Ag_3PO_4: 534 nm; g-C_3N_4: 484 nm). Profiting from the urea treatment, all the
300 absorption edges of single-phase urea-treated semiconductors appeared considerably
301 red-shifted, in comparison with the untreated controls (Ag_3PO_4: 526 nm; g-C_3N_4: 475
302 nm) (Fig. 3A). Combining with the appreciably increased carrier density calculated
303 from the Mott-Schottky curves [47] after urea treatment (Fig. S6), all the results
304 indicated higher fraction of light absorption and higher photoinduced charge generation
305 for the urea-treated heterojunction. The band gaps (E_g) and other energy level
306 information of the single-phase semiconductors were estimated through Tauc plots [48]
307 (Fig. 3B) and Mott-Schottky curves [47] (Fig. S6), and summarized in Table S2.
308 Specially, two energy gaps (2.32 eV and 2.24 eV) of the urea-treated Ag_3PO_4 were

309 acquired from its Tauc plot, corresponding to the two intercepts in its Mott-Schottky
310 curve (Fig. S6B), consistent with the same observation of the CeF_3 photocatalyst with
311 an introduced IB [16]. The broader 2.32 eV between the VB and CB was the intrinsic
312 band gap of Ag_3PO_4, while the narrower 2.24 eV was a new energy state between the
313 CB and IB of about 0.08 eV below the CB of Ag_3PO_4 originated from urea treatment.
314 These observations confirmed that a two-step optical transition with the first transition
315 from VB to IB and the second from IB to CB existed in the photogenerated charges
316 transfer process of the urea-treated Ag_3PO_4.

317 **Here Fig. 3**

318 Profiting from the introduced IB by urea treatment, the transient photocurrent of
319 the urea-treated Ag_3PO_4 (0.82 μA) was 2.1-fold of the untreated control (0.39 μA) (Fig.
320 3C). After combination with g-C_3N_4, the photocurrent of the heterojunction with urea
321 treatment sharply increased to 10.42 μA, and was 2.5-fold of the untreated Ag_3PO_4/g-
322 C_3N_4 (4.14 μA), indicating the lower recombination of photogenerated charges after
323 urea treatment. A strong emission peak at about 475 nm was observed in the PL spectra
324 of the pure g-C_3N_4 nanosheets (Fig. 3D), consistent with the corresponding band gap
325 of about 2.6 eV [49], while the peak intensity of Ag_3PO_4/g-C_3N_4 was appreciably
326 reduced due to the non-emission of Ag_3PO_4. The PL intensities of all urea-treated
327 samples were obviously suppressed, compared to the controls, confirming again the
328 recombination of photogenerated charge carriers was efficiently mitigated by urea
329 treatment. Interestingly, a new emission peak appeared at 554 nm in the PL spectra of
330 Ag_3PO_4 and Ag_3PO_4/g-C_3N_4 after urea treatment, corresponding to a new energy state

of 2.24 eV, which was generally attributed to the recombination of photoinduced holes in VB and the electrons trapped in the IB of Ag_3PO_4 [16,49]. Conversely, the lack of peaks in the PL spectra of urea-untreated Ag_3PO_4-based photocatalysts [12], reflected the role of urea treatment in improvement of photocatalytic activity. Combining with the Mott-Schottky, PL and Tauc plots, all results strongly indicated the formation of IB in Ag_3PO_4, which have been generally regarded as sufficient evaluation criteria for IB photocatalyst [13,16]. Therefore, the two-step optical transition was again substantiated in the urea-treated Ag_3PO_4. According to the above results, the new energy state within the band gap of Ag_3PO_4 induced by urea treatment acted as traps for the photoinduced carriers and intermediate transition platform, thus preventing the recombination of electron-hole pairs and decelerating photoinduced charge transfer, ultimately alleviating redundant electrons accumulation on the CB of Ag_3PO_4, suppressing the occurrence of photocorrosion and thus enhancing the photocatalytic performance of the photo-assisted MES.

Electrochemically active substances (such as flavin and outer membrane *c*-type cytochromes) from electrotrophs contributed to the variation of DPV peaks [50], while EIS analysis provided sufficient information on material and surface properties of the electrodes, electrotroph metabolism and electron transfer mechanisms [51]. DPV plots and EIS analysis (Fig. 3E and F; Table S3; equivalent circuit (Fig. S7)) were thus employed to assess the influence of electrochemical activities for the bio-photocathodes caused by urea treatment. All the biotic photocathodes exhibited two DPV peaks, one of which at about −0.52 V was ascribed to the reduction of inorganic carbon for acetate

353 production [2,8,52], while the other at about 0.02 V was related to outer membrane *c*-
354 type cytochromes [8,50]. The stronger reduction peak current (−2.55 mA) of the urea-
355 treated Ag_3PO_4/g-C_3N_4 along with the more positive reduction onset potential (−0.28
356 V) and the lower charge transfer resistance (R_{ct}, 26 Ω), indicated the more powerful
357 reducing power and the faster charge transfer rate for inorganic carbon reduction, in
358 comparison with the urea-treated Ag_3PO_4 (current: −1.61 mA; potential: −0.31 V; R_{ct}:
359 40 Ω) or g-C_3N_4 (current: −1.51 mA; potential: −0.32 V; R_{ct}: 67 Ω), or the untreated
360 Ag_3PO_4/g-C_3N_4 (current:−2.04 mA; potential: −0.30 V; R_{ct}: 31 Ω). The noticeably
361 favorable electrochemical parameters of the urea-treated single-phase semiconductors
362 and of the combined phases in the heterojunction suggested the influential role of
363 pyrrolic N and of the IB introduced by urea treatment for augmenting the extracellular
364 electron transfer and the photocatalytic electrons transfer processes. Moreover, the
365 obviously higher reduction peak around 0.02 V of the urea-treated g-C_3N_4 and
366 Ag_3PO_4/g-C_3N_4 demonstrated that a higher fraction of outer membrane *c*-type
367 cytochromes participated in the extracellular electron transfer for preferable system
368 performance [50], in comparison with the untreated controls. These excellent
369 electrochemical activities for the bio-photocathodes profited from the strongest affinity
370 and the lowest adsorption energy of the increased pyrrole N content to the central
371 functional porphyrin iron of the outer membrane *c*-type cytochromes [20,21], where
372 pyrrole N content acted as a more effective electron active site for producing a higher
373 amount of reducing equivalents, such as H_2 generation, and a superior platform for
374 electrons transfer to *S. marcescens* for photo-assisted inorganic carbon reduction. These

results were consistent with the enhanced extracellular electron transfer caused by a pyrrolic N-enriched graphitic carbon scaffold electrode that yielded higher bioelectricity generation in microbial fuel cells [21] and with the increased activity using a three-dimensional N-doped macroporous carbon foam electrode with a high pyrrolic N content [53]. The DPV electrochemical pattern of the abiotic urea-treated Ag_3PO_4/g-C_3N_4 control showing no peaks (Fig. 3E), further reflected the role of *S. marcescens* in acetate production from inorganic carbon reduction.

3.3 MES performance and suppression of photocorrosion

As the core component of the photo-assisted MES, the energy levels and configurations of photocatalysts significantly affected the acetate production in the bio-photocathodes. According to the highest acetate production rate and $CE_{acetate}$, the optimal operating parameters were set at a urea concentration of 3.28 g/L (Fig. S8), a molar ratio of Ag_3PO_4 to g-C_3N_4 of 1: 2 (Fig. S9) and a photocatalyst loading amount of 0.43 mg/cm^2 (Fig. S10). Benefiting from synergistic interaction of the new energy state as IB and the higher pyrrolic N content induced by urea treatment, the urea-treated Ag_3PO_4/g-C_3N_4 photocathode achieved 80% higher acetate production rate of 9.7 ± 0.3 mM/d along with an optimal $CE_{acetate}$ of 98 ± 2%, a solar-to-acetate efficiency of 1.16 ± 0.03% and an overall energy efficiency of 0.94 ± 0.02% over 0.5 d operation (Fig. 4A, C, D and Fig. S11A), in comparison with the untreated heterojunction (acetate: 5.4 ± 0.1 mM/d; $CE_{acetate}$: 93 ± 2%; ξ: 0.64 ± 0.01%; η: 0.57 ± 0.01%). The improved system performance with the urea-treated Ag_3PO_4 or g-C_3N_4 photocathodes than the corresponding untreated controls were attributed to the concerted effect occurring on

each single semiconductors, namely the mid-gap state formed in the band-gap of Ag_3PO_4 and the enhanced pyrrolic N content resulting on the g-C_3N_4. In addition, the higher total reducing equivalent H_2 observed under the open circuital conditions (OCCs) (Fig. S11B), contrasted sharply with the lower residual H_2 and significantly higher acetate production (Fig. 4B) observed under closed circuital conditions (CCCs), indicated the essential mediation of H_2 in the inorganic carbon reduction via the Wood-Ljungdahl pathway for acetate production [1-4].

Here Fig. 4

Interestingly, four characteristic peaks (38.1°, 44.5°, 64.4°, 77.6°) ascribed to metallic Ag (JCPDS No.04−0783) [10,54] and detected in the XRD profile of the untreated Ag_3PO_4/g-C_3N_4 under OCCs (Fig. 4E), reflected the occurrence of photocorrosion. In contrast, no characteristic peak of metallic Ag was observed in either the urea-treated Ag_3PO_4/g-C_3N_4 photocathodes or the untreated heterojunction under CCCs. These were further proven by the XPS results (Fig. 4F), where two new peaks at 367.6 eV and 373.5 eV corresponding to metallic Ag [10,54] only appeared in the Ag 3d high resolution spectra of the urea-untreated Ag_3PO_4/g-C_3N_4 under OCCs. These results collectively confirmed the photocorrosion of Ag_3PO_4 was efficiently prevented in both Ag_3PO_4/g-C_3N_4 with or without urea treatment under CCCs and the urea-treated Ag_3PO_4/g-C_3N_4 under OCCs. Differing from the suppression of photocorrosion by the in-situ consumption of H_2O_2 over the untreated Ag_3PO_4/g-C_3N_4 with the necessary need of having a closed circuit [8], the urea-treated heterojunction restrained the photocorrosion even under OCCs due to the synergistic interaction of IB and pyrrolic

N caused by urea treatment, thus contributing to high-efficient and stable acetate production in the Ag_3PO_4/g-C_3N_4 photocathode MES.

3.4 Photocatalytic mechanism over urea-treated Ag_3PO_4/g-C_3N_4 photocathode

The above analysis suggests a photocatalytic mechanism of the urea-treated Ag_3PO_4/g-C_3N_4 photocathode as shown in Fig. 5. Under visible light illumination, both Ag_3PO_4 and g-C_3N_4 semiconductors are excited to generate hole-electron pairs, and photogenerated electrons can be transferred from the VB to the corresponding CB. The photoinduced charges transfer process in the Ag_3PO_4 phase of the heterojunction, however, can benefit from the mid-gap IB introduced by urea treatment, besides its intrinsic electron excitation from VB to CB. Therefore, a two-step optical electron transition can take place, with the first transition from VB to IB and the second from IB to CB with higher carrier density and decelerated photoinduced charge transfer. The electrons undergoing the two-step transition onto the CB or IB of Ag_3PO_4 with a decelerated transfer, prefer to recombine with the holes in the VB of g-C_3N_4 at the interface of the heterojunction via the Z-scheme charge transfer mechanism. As a result, such recombination process prevents the excessive accumulation of electrons on the CB of Ag_3PO_4 which aversely caused Ag^+ photocorrosion. Simultaneously, a fraction of the photogenerated reductive electrons on the CB of g-C_3N_4 can be directly transferred to the *S. marcescens* electrotroph via pyrrolic N of g-C_3N_4 (direct electron transfer), while the residual photoinduced electrons can be utilized for H_2 evolution at pyrrolic N active sites, which in turn is metabolized in-situ by the electrotroph acting as an electron carrier mediator (indirect electron transfer). Ultimately, the electrons (via

441 direct and indirect routes) and bicarbonate are metabolized by the *S. marcescens*
442 electrotroph for efficient acetate production through the Wood-Ljungdahl pathway [1-
443 4]. Concurrently, the holes left on the VB of Ag_3PO_4 can be refilled by the electrons
444 arriving from the external circuit to draw a higher current. The above mechanism, using
445 a pyrrolic N enriched Ag_3PO_4/g-C_3N_4 photocathode with an IB in a photo-assisted MES,
446 realizes a highly efficient and photostable acetate production and successfully
447 prevented the spontaneous photocorrosion of the Ag_3PO_4 semiconductor in the
448 Ag_3PO_4/g-C_3N_4 heterojunction.

449 **Here Fig. 5**

450 *3.5 Continuous acetate production process*

451 The rate of acetate production and the $CE_{acetate}$ during each batch cycle in the MES
452 reactor remained constant up to 0.5 d operation after which a decrease was observed
453 along with a sharp increased R_{dif} caused by the insufficient supply of inorganic carbon
454 (Fig. S12; Table S4), as also shown in other studies [55]. Therefore, the reactor was
455 supplemented with a new dose of bicarbonate after each 0.5 d, to guarantee adequate
456 supply of inorganic carbon in the reactor for acetate production over 12 days continuous
457 operation. The urea-treated Ag_3PO_4/g-C_3N_4 photocathodes almost linearly accumulated
458 acetate up to 115 ± 1 mM (average acetate production rate: 9.6 ± 0.1 mM/d) over the
459 continuous 12 days operation, along with negligible changes of $CE_{acetate}$ (95 ± 3%), ξ
460 (1.15 ± 0.04%), and η (0.94 ± 0.03%) (Fig. 6A−C and Fig. S13A). These values were
461 insignificantly different from the inchoate performance at 0.5 d operation (acetate: 9.7
462 ± 0.3 mM/d, p: 0.782; $CE_{acetate}$: 98 ± 2%, p: 0.493; ξ: 1.16 ± 0.03%, p: 0.698; η: 0.94 ±

463 0.02%, *p*: 1.00), and indicated a highly stable and efficient performance of the urea-
464 treated Ag_3PO_4/g-C_3N_4 photocathode. The impact of the urea treatment method on the
465 Ag_3PO_4/g-C_3N_4 photocathode can also be quantified by a net increase of the 82 ± 2%
466 of the acetate accumulated in the reactor after 12 d operation (Fig. 6A). These values
467 appreciably exceeded those obtained by the $BiVO_4$/Mo photoanode with a mix-culture
468 CHT/Ni foam biocathode (acetate: 0.9 ± 0.2 mM/d; $CE_{acetate}$: 62 ± 12%; ξ: 0.97 ± 0.19%)
469 [56], or the Cr_2O_3/Ru-$SrTiO_3$:La,Rh/ITO/RuO_2-$BiVO_4$:Mo photocatalyst sheets with
470 *Sporomusa ovata* (acetate: 0.15 ± 0.02 mM/d; ξ: 0.70 ± 0.04%) [57] and also exceeded
471 the values obtained using a WO_3/MoO_3/g-C_3N_4 (acetate: 3.1 ± 0.2 mM/d; ξ: 0.37 ±
472 0.05%) [2] or a urea-treated $MnFe_2O_4$/g-C_3N_4 (acetate: 8.5 ± 0.6 mM/d; ξ: 1.02 ± 0.06%)
473 [6] photocathode in the same MES (Table S5). The poor system performance with the
474 bare graphite felt control (acetate: 1.3 ± 0.2 mM/d; $CE_{acetate}$: 51 ± 6%) highlighted the
475 essential and profitable role of photocatalysis in this photo-assisted MES.
476 The absence of the characteristic peak of metallic Ag in the Ag 3d high resolution
477 XPS spectra for the urea-treated Ag_3PO_4/g-C_3N_4 photocathode after 12 days operation
478 (Fig. 6F), confirmed that the photocorrosion of the photocatalysts was efficiently
479 inhibited. Nearly same XRD results as Fig. 4E also indicated the always inhibition of
480 photocorrosion of the photocathode (data not shown). Combining these results with a
481 significant reduction of catalysts leaching to the insignificant value of less than 1% (Fig.
482 6D), slight increase in internal resistance (Fig. 6E; Table S6), as well as unchanged
483 elementary compositions and morphology (Fig. S13B and C) between the fresh and
484 used photocathodes, collectively this study demonstrated the excellent robustness and

chemical stability of this urea-treated Ag_3PO_4/g-C_3N_4 photocathode.

Here Fig. 6

In general, introduction of IB into semiconductors with controllable band structure and tunable charge transfer to inhibit the occurrence of photocorrosion is not limited to Ag_3PO_4 and may also be applicable to many other photocatalysts (e.g., CdS, CuO_2 and other Ag^+-based semiconductors) in the anti-photocorrosion field [11]. The two-step optical transition mediated by the introduced IB can function as an intermediate transition platform to decelerate photoinduced charge transfer and simultaneously alleviate redundant electrons accumulation on the CB of the single semiconductor [13-16], ultimately suppressing the photocorrosion to improve the photostability and durability of the photocatalysts. In addition, adjusting N configuration of g-C_3N_4-based photocatalysts by ingenious and rational design opens a new insight to other bio-abiotic hybrid systems for improving the interaction between photocathodes/photosensitizers and electrotrophs, where the CB of the pyrrolic nitrogen enriched g-C_3N_4 acted as an electrons donor and transfer platform for enhancing the photocatalytic performance.

4 Conclusions

In summary, in this study Ag_3PO_4 and g-C_3N_4 were strategically pre-treated with urea to introduce an intermediary mid-gap band in the Ag_3PO_4 electronic structure and an improvement in pyrrolic N content in the g-C_3N_4 semiconductor, compared to the untreated controls. Benefitting from the synergistic effect of such IB and pyrrolic N, the urea-treated Ag_3PO_4/g-C_3N_4 heterojunction immobilized on a photocathode

achieved a significant acetate production rate of 9.6 ± 0.1 mM/d over a continuous 12 days operation, along with a $CE_{acetate}$ of 95 ± 3% and a ξ of 1.15 ± 0.04%. As a result of this material synthesis strategy, the acetate production rate and the ξ increased by up to 1.8-fold in comparison to the untreated pristine Ag_3PO_4/g-C_3N_4 controls. The photocorrosion of Ag_3PO_4/g-C_3N_4 was effectively suppressed by a two-step charge transfer pathway mediated by the introduced IB which prevented the excessive accumulation of electrons in the conduction band of Ag_3PO_4, while the pyrrole N acted as an effective electron active site for increasing the evolution of H_2 and superior platform for electrons transfer to the *S. marcescens* electrotroph. The above mechanism ultimately achieved a stable and high-efficient acetate production from inorganic carbon reduction in the urea-treated Ag_3PO_4/g-C_3N_4 photocathode MES. This study provides new insights for the ingenious synthesis of highly effective photocatalysts and their combination with MESs for the sustainable conversion of inorganic carbon (CO_2 or HCO_3^-) to a key block chemical (acetate) using visible light in photo-assisted MESs, thus promoting the development of a circular economy and net-zero processes.

Ethical Statement

Compliance with Ethical Standards.

Conflict of interest

The authors declare no competing interests

Acknowledgements

The authors gratefully acknowledge financial support from the National Natural Science Foundation of China (Nos. 22276025 and 52070032).

References

[1] S. Cestellos-Blanco, H. Zhang, J.M. Kim, Y.X. Shen, P. Yang, Photosynthetic semiconductor biohybrids for solar-driven biocatalysis, Nat. Catal. 45 (2020) 245–255. https://doi.org/10.1038/s41929-020-0428-y

[2] Z. Cai, L. Huang, X. Quan, Z. Zhao, Y. Shi, G. Li-Puma, Acetate production from inorganic carbon (HCO_3^-) in photo-assisted biocathode microbial electrosynthesis systems using WO_3/MoO_3/g-C_3N_4 heterojunctions and *Serratia marcescens*

species, Appl. Catal. B-Environ. 267 (2020) 118611. https://doi.org/10.1016/j.apcatb.2020.118611
[3] Y. Su, S. Cestellos-Blanco, J.M. Kim, Y. Shen, Q. Kong, D. Lu, C. Liu, H. Zhang, Y. Cao, P. Yang, Close-packed nanowire-bacteria hybrids for efficient solar-driven CO_2 fixation, Joule 4 (2020) 800–811. https://doi.org/10.1016/j. joule.2020.03.001
[4] N.S. Weliwatte & S.D. Minteer, Photo-bioelectrocatalytic CO_2 reduction for a circular energy landscape, Joule 5 (2021) 2564–2592. https://doi.org/10.1016/j.joule.2021.08.003
[5] T. Song, T. Li, R. Tao, H. Huang, J. Xie, CuO/g-C_3N_4 heterojunction photocathode enhances the microbial electrosynthesis of acetate through CO_2 reduction, Sci. Total Environ. 818 (2022) 151820. https://doi.org/10.1016/j.scitotenv.2021.151820
[6] W. Kong, L. Huang, X. Quan, G. Li-Puma, Synergistic induced charge transfer switch by oxygen vacancy and pyrrolic nitrogen in $MnFe_2O_4$/g-C_3N_4 heterojunctions for efficient transformation of bicarbonate to acetate in photo-assisted MES, Appl. Catal. B-Environ. 307 (2022) 121214. https://doi.org/10.1016/j.apcatb.2022.121214
[7] T. Li, K. Zhang, D. Luo, T. Song, J. Xie, CuO/g-C_3N_4/rGO multifunctional photocathode with simultaneous enhancement of electron transfer and substrate mass transfer facilitates microbial electrosynthesis of acetate, Int. J. Hydrogen Energ. 47 (2022) 34875–34886. https://doi.org/10.1016/j.ijhydene.2022.08.066
[8] W. Kong, L. Huang, X. Quan, Z. Zhao, G. Li-Puma, Efficient production of acetate from inorganic carbon (HCO_3^-) in microbial electrosynthesis systems incorporating Ag_3PO_4/g-C_3N_4 anaerobic photo-assisted biocathodes, Appl. Catal. B-Environ. 284 (2021) 119696. https://doi.org/10.1016/j.apcatb.2020.119696
[9] X. Yang, L. Tian, X. Zhao, H. Tang, Q. Liu, G. Li, Interfacial optimization of g-C_3N_4-based Z-scheme heterojunction toward synergistic enhancement of solar-driven photocatalytic oxygen evolution, Appl. Catal. B-Environ. 244 (2019) 240–249. https://doi.org/10.1016/j.apcatb.2018.11.056
[10] M. Ding, J. Zhou, H. Yang, R. Cao, S. Zhang, M. Shao, X. Xu, Synthesis of Z-scheme g-C_3N_4 nanosheets/Ag_3PO_4 photocatalysts with enhanced visible-light photocatalytic performance for the degradation of tetracycline and dye, Chin. Chem. Lett. 31 (2020) 71–76. https://doi.org/10.1016/j.cclet.2019.05.029
[11] B. Wong, M. Qi, C. Han, Z. Tang, Y. Yu, Photocorrosion inhibition of semiconductor-based photocatalysts: basic principle, current development, and future perspective, ACS Catal. 9 (2019), 4642–4687. https://doi.org/10.1021/acscatal.9b00313
[12] M. Sun, Q. Zeng, X. Zhao, Y. Shao, P. Ji, C. Wang, T. Yan, B. Du, Fabrication of novel g-C_3N_4 nanocrystals decorated Ag_3PO_4 hybrids: Enhanced charge separation and excellent visible-light driven photocatalytic activity, J. Hazard. Mater. 339 (2017) 9–21. https://doi.org/10.1016/j.jhazmat.2017.06.003
[13] L. Liang, X. Li, Y. Sun, Y. Tan, X. Jiao, H. Ju, Z. Qi, J. Zhu, Y. Xie, Infrared light-driven CO_2 overall splitting at room temperature, Joule 2 (2018) 1004–1016. https://doi.org/10.1016/j.joule.2018.02.019

[14] J. Wang, C. Cao, Y. Zhang, Y. Zhang, L. Zhu, Underneath mechanisms into the super effective degradation of PFOA by BiOF nanosheets with tunable oxygen vacancies on exposed (101) facets, Appl. Catal. B-Environ. 286 (2021) 119911. https://doi.org/10.1016/j.apcatb.2021.119911

[15] R. Jaiswal, J. Bharambe, N. Patel, A. Dashora, D.C. Kothari, A. Miotello, Copper and nitrogen co-doped TiO_2 photocatalyst with enhanced optical absorption and catalytic activity, Appl. Catal. B-Environ. 168–169 (2015) 333–341. https://doi.org/10.1016/j.apcatb.2014.12.053

[16] B. Han, S. Yu, D. Zhao, Y. Lou, J. Gao, Z. Liu, Z. Wang, G. Qian, Hyper oxygen incorporation in CeF_3: a new intermediate-band photocatalyst for antibiotic degradation under visible/NIR light, RSC Adv. 10 (2020) 38798. https://doi.org/10.1039/d0ra06107g

[17] M. Song, M. Du, Q. Liu, F. Xing, C. Huang, X. Qiu, Enhancement of photocatalytic activities in hierarchical BiOBr microflowers induced by oxygen vacancies, Catal. Today 335 (2019) 193–199. https://doi.org/10.1016/j.cattod.2018.11.006

[18] S. Li, S. Shi, G. Huang, Y. Xiong, S. Liu, Synergetic tuning charge dynamics and potentials of Ag_3PO_4 photocatalysts with boosting activity and stability by facile in-situ fluorination, Appl. Surf. Sci. 455 (2018) 1137–1149. https://doi.org/10.1016/j.apsusc.2018.06.027

[19] V.W.H. Lau, V.W.Z. Yu, F. Ehrat, T. Botari, I. Moudrakovski, T. Simon, V. Duppel, E. Medina, J.K. Stolarczyk, J. Feldmann, V. Blum, B.V. Lotsch, Urea-modified carbon nitrides: enhancing photocatalytic hydrogen evolution by rational defect engineering, Adv. Energy Mater. 7 (2017) 1602251. https://doi.org/10.1002/aenm.201602251

[20] X. Liu, X. Sun, J. Chen, Y. Huang, J. Xie, W. Li, G. Sheng, Y. Zhang, F. Zhao, R. Lu, H. Yu, Phenothiazine derivative-accelerated microbial extracellular electron transfer in bioelectrochemical system, Sci. Rep. 3 (2013) 1616. https://doi.org/10.1038/srep01616

[21] S. You, M. Ma, W. Wang, D. Qi, X. Chen, J. Qu, N. Ren, 3D macroporous nitrogen-enriched graphitic carbon scaffold for efficient bioelectricity generation in microbial fuel cells, Adv. Energy Mater. 7 (2017) 1601364. https://doi.org/10.1002/aenm.201601364

[22] Y. Xu, Y. Mo, J. Tian, P. Wang, H. Yu, J. Yu, The synergistic effect of graphitic N and pyrrolic N for the enhanced photocatalytic performance of nitrogen-doped graphene/TiO_2 nanocomposites, Appl. Catal. B-Environ. 181 (2016) 810–817. https://doi.org/10.1016/j.apcatb.2015.08.049

[23] R. Shi, Z. Li, H. Yu, L. Shang, C. Zhou, G.I.N. Waterhouse, L. Wu, T. Zhang, Effect of nitrogen doping level on the performance of N-doped carbon quantum dot/TiO_2 composites for photocatalytic hydrogen evolution, ChemSusChem 10 (2017) 4650–4656. https://doi.org/10.1002/cssc.201700943

[24] Q. Wang, L. Huang, X. Quan, G. Li-Puma, Sequential anaerobic and electro-Fenton processes mediated by W and Mo oxides for degradation/mineralization of azo dye methyl orange in photo assisted microbial fuel cells, Appl. Catal. B-

Environ. 245 (2019) 672–680. https://doi.org/10.1016/j.apcatb.2019.01.026
[25] Y. Qian, L. Huang, P. Zhou, F. Tian, G. Li-Puma, Reduction of Cu(II) and simultaneous production of acetate from inorganic carbon by *Serratia marcescens* biofilms and plankton cells in microbial electrosynthesis systems, Sci. Total Environ. 666 (2019) 114–125. https://doi.org/10.1016/j.scitotenv.2019.02.267
[26] C. Karthikeyan, S. Rajeswari, S. Maruthamuthu, K. Subramanian, G. Rajagopal, Biogenic ammonia for CO_2 capturing and electrochemical conversion into bicarbonate and formate, J. CO_2 Util. 6 (2014) 53–61. https://doi.org/10.1016/j.jcou.2014.03.004
[27] G. Upendar, A.N. Mistry, S.G. Thakurata, J. Chakrabarty, K.C. Ghanta, S. Dutta, Carbon dioxide biofixation using microorganisms and assessment of biofuel production, Environ. Prog. Sustain. Energy 37 (2018) 11594–1600. https://doi.org/10.1002/ep.12835
[28] I. Salmerón, C.L.A. Guzmán, V.H.R. Sánchez, I.P. Reyes, J.S. Mata, S.C. Cueva, Hydrogen and alcohols production by *Serratia* sp. from an inorganic carbon source, J. CO_2 Util. 58 (2022) 101914. https://doi.org/10.1016/j.jcou.2022.101914
[29] L. Huang, X. Xing, P. Zhou, G. Li-Puma, Mixotrophic bacteria for environmental detoxification of contaminated waste and wastewater, Appl. Microbiol. Biotechnol. 105 (2021) 6627–6648. https://doi.org/10.1007/s00253-021-11514-5
[30] D. Zee, T, Chantarojsiri, J.R. Long, C.J. Chang, Metal-polypyridyl catalysts for electro- and photochemical reduction of water to hydrogen, Acc. Chem. Res. 48 (2015) 2027–2036. https://doi.org/10.1021/acs.accounts.5b00082
[31] T. Waly, M.D. Kennedy, G.J. Witkamp, G. Amy, J.C. Schippers, Predicting and measurement of pH of seawater reverse osmosis concentrates, Desalination 280 (2011) 27–32. https://doi.org/10.1016/j.desal.2011.06.057
[32] L. Jourdin, T. Grieger, J. Monetti, V. Flexer, S. Freguia, Y. Lu, J. Chen, M. Romano, G.G. Wallace, J. Keller, High acetic acid production rate obtained by microbial electrosynthesis from carbon dioxide, Environ. Sci. Technol. 49 (2015), 13566–13574. https://doi.org/10.1021/acs.est.5b03821
[33] R. Gonzalez-Olmos, S. Puig, R. Gonzalez-Olmos, M.D. Balaguer, J. Colprim, Continuous acetate production through microbial electrosynthesis from CO_2 with microbial mixed culture, J. Chem. Technol. Biotechnol. 91 (2016) 921–927. https://doi.org/10.1002/jctb.4657
[34] S. Wang, L. Huang, L. Gan, X. Quan, N. Li, G. Chen, L. Lu, D. Xing, F. Yang, Combined effects of enrichment procedure and non-fermentable or fermentable co-substrate on performance and bacterial community for pentachlorophenol degradation in microbial fuel cells, Bioresour. Technol. 120 (2012) 120–126. https://doi.org/10.1016/j.biortech.2012.06.022
[35] S. Gildemyn, K. Verbeeck, R. Slabbinck, S.J. Andersen, A. Prevoteau, K. Rabaey, Integrated production, extraction, and concentration of acetic acid from CO_2 through microbial electrosynthesis, Environ. Sci. Technol. Lett. 2 (2015) 325–328. https//doi.org/10.1021/acs.estlett.5b00212
[36] L. Jourdin, S. Freguia, V. Flexer, J. Keller, Bringing high-rate, CO_2-based microbial electrosynthesis closer to practical implementation through improved

668 electrode design and operating conditions, Environ. Sci. Technol. 50 (2016) 1982–
669 1989. https://doi.org/10.1021/acs.est.5b04431
670 [37] J. Li, Z. Li, S. Xiao, Q. Fu, H. Kobayashi, L. Zhang, Q. Liao, X. Zhu, Startup
671 cathode potentials determine electron transfer behaviours of biocathodes
672 catalysing CO_2 reduction to CH_4 in microbial electrosynthesis, J. CO_2 Util. 35
673 (2020) 169–175. https://doi.org/10.1016/j.jcou.2019.09.013
674 [38] S.B. Velasquez-Orta, T.P. Curtis, B.E. Logan, Energy from algae using microbial
675 fuel cells. Biotechnol. Bioeng. 103 (2009) 1068–1076.
676 https://doi.org/10.1002/bit.22346
677 [39] B.E. Logan, Essential data and techniques for conducting microbial fuel cell and
678 other types of bioelectrochemical systems experiments, ChemSusChem 5 (2012)
679 988–994. https://doi.org/10.1002/cssc.201100604
680 [40] L. Huang, Y. Liu, L. Yu, X. Quan, G. Chen, A new clean approach for production
681 of cobalt dihydroxide from aqueous Co(II) using oxygen-reducing biocathode
682 microbial fuel cells, J. Clean. Prod. 86 (2015) 441–446.
683 https://doi.org/10.1016/j.jclepro.2014.08.018
684 [41] M.E. Demir, G. Chehade, I. Dincer, B. Yuzer, H. Selcuk, Design and analysis of a
685 new system for photoelectrochemical hydrogen production from wastewater,
686 Energy Convers. Manag. 199 (2019) 111903.
687 https://doi.org/10.1016/j.enconman.2019.111903
688 [42] R. Li, M. Cai, Z. Xie, Q. Zhang, Y. Zeng, H. Liu, G. Liu, W. Lv, Construction of
689 heterostructured $CuFe_2O_4$/g-C_3N_4 nanocomposite as an efficient visible light
690 photocatalyst with peroxydisulfate for the organic oxidation, Appl. Catal. B-
691 Environ. 244 (2019) 974–982. https://doi.org/10.1016/j.apcatb.2018.12.043
692 [43] P. Niu, J. Dai, X. Zhi, Z. Xia, S. Wang, L. Li, Photocatalytic overall water splitting
693 by graphitic carbon nitride, InfoMat 3 (2021) 931–936.
694 https://doi.org/10.1002/inf2.12219
695 [44] H. Wang, X. Liu, P. Niu, S. Wang, J. Shi, L. Li, Porous two-dimensional materials
696 for photocatalytic and electrocatalytic applications, Matter 2 (2020) 1377–1413.
697 https://doi.org/10.1016/j.matt.2020.04.002
698 [45] W. Lai, Z. Chen, S. Ye, Y. Xu, G. Xie, C. Kuang, Y. Li, L. Zheng, L. Wei, $BiVO_4$
699 prepared by the sol–gel doped on graphite felt cathode for ciprofloxacin
700 degradation and mechanism in solar-photo-electro-Fenton, J. Hazard. Mater. 408
701 (2021) 124621. https://doi.org/10.1016/j.jhazmat.2020.124621
702 [46] W. Chang, W. Xue, E. Liu, J. Fan, B. Zhao, Highly efficient H_2 production over
703 $NiCo_2O_4$ decorated g-C_3N_4 by photocatalytic water reduction, Chem. Eng. J. 362
704 (2019) 392–401. https://doi.org/10.1016/j.cej.2019.01.021
705 [47] F. Meng, J. Li, S.K. Cushing, M. Zhi, N. Wu, Solar hydrogen generation by
706 nanoscale p-n junction of p-type molybdenum disulfide/n-type nitrogen-doped
707 reduced graphene oxide, J. Am. Chem. Soc. 135 (2013) 10286–10289.
708 https://doi.org/10.1021/ja404851s
709 [48] J. Tauc, Optical properties and electronic structure of amorphous, Mater. Res. Bull.
710 3 (1968) 37. https://doi.org/10.1016/0025-5408(68)90023-8
711 [49] J. Wang, Y. Xia, H. Zhao, G. Wang, L. Xiang, J. Xu, S. Komarneni, Oxygen

defects-mediated Z-scheme charge separation in g-C_3N_4/ZnO photocatalysts for enhanced visible-light degradation of 4-chlorophenol and hydrogen evolution, Appl. Catal. B-Environ. 206 (2017) 406–416. https://doi.org/10.1016/j.apcatb.2017.01.067

[50] Y. Xiao, E. Zhang, J. Zhang, Y. Dai, Z. Yang, H.E.M. Christensen, J. Ulstrup, F. Zhao, Extracellular polymeric substances are transient media for microbial extracellular electron transfer, Sci. Adv. 3 (2017) e1700623. https://doi.org/10.1126/sciadv.1700623

[51] X. Dominguez-Benetton, S. Sevda, K. Vanbroekhoven, D. Pant, The accurate use of impedance analysis for the study of microbial electrochemical systems, Chem. Soc. Rev. 41 (2012) 7228–7246. https://doi.org/10.1039/c2cs35026b

[52] C.W. Marshall, D.E. Ross, E.B. Fichot, R.S. Norman, H.D. May, Long-term operation of microbial electrosynthesis systems improves acetate production by autotrophic microbiomes, Environ. Sci. Technol. 47 (2013) 6023–6029. https://doi.org/10.1021/es400341b

[53] Y. Wang, C. He, W. Li, W. Zong, Z. Li, L. Yuan, G. Wang, Y. Mu, High power generation in mixed-culture microbial fuel cells with corncob-derived three-dimensional N-doped bioanodes and the impact of N dopant states, Chem. Eng. J. 399 (2020) 125848. https://doi.org/10.1016/j.cej.2020.125848

[54] T. Cai, L. Wang, Y. Liu, S. Zhang, W. Dong, H. Chen, X. Yi, J. Yuan, X. Xia, C. Liu, S. Luo, Ag_3PO_4/Ti_3C_2 MXene interface materials as a Schottky catalyst with enhanced photocatalytic activities and anti-photocorrosion performance, Appl. Catal. B-Environ. 263 (2018) 545–554. https://doi.org/10.1016/j.apcatb.2018.08.053

[55] G. Mohanakrishna, K. Vanbroekhoven, D. Pant, Impact of dissolved carbon dioxide concentration on the process parameters during its conversion to acetate through microbial electrosynthesis, React. Chem. Eng. 3 (2018) 371–378. https://doi.org/10.1039/c7re00220c

[56] B. Bian, L. Shi, K.P. Katuri, J. Xu, P. Wang, P. E. Saikaly, Efficient solar-to-acetate conversion from CO_2 through microbial electrosynthesis coupled with stable photoanode, Appl. Energ. 278 (2020) 115684. https://doi.org/10.1016/j.apenergy.2020.115684

[57] Q. Wang, S. Kalathil, C. Pornrungroj, C.D. Sahm, E. Reisner, Bacteria-photocatalyst sheet for sustainable carbon dioxide utilization, Nat. Catal. 5 (2022) 633–641. https://doi.org/10.1038/s41929-022-00817-z

Fig. 1 XRD patterns (A), high resolution XPS spectra of N 1s (B) and O 1s (C) and ESR spectra (D) of various fresh photocatalysts.

Fig. 2 SEM images of Ag_3PO_4/g-C_3N_4 cathodes with (A) or without (B) urea treatment, and urea-treated Ag_3PO_4/g-C_3N_4 cathode after incorporating with *S. marcescens* (C). Elemental mapping images (D–H) and EDS (I) spectra of the urea-treated Ag_3PO_4/g-C_3N_4.

Fig. 3 UV-vis DRS spectra (A), Tauc plots (B), transient photocurrent responses (C) and PL spectra (D) of various photocatalysts. DPVs (E) and Nyquist plots of EIS (F) of

different *S. marcescens* photocathodes and abiotic Ag_3PO_4/g-C_3N_4 photocathode.

Fig. 4 Acetate production (A), residual H_2 (B), $CE_{acetate}$ (C) and solar-to-acetate efficiency (D) of different photocathodes with *S. marcescens* (operational time: 0.5 d). XRD patterns (E) and Ag 3d high resolution XPS spectra (F) of Ag_3PO_4/g-C_3N_4 cathodes with or without urea treatment under various conditions after 0.5 d operation.

Fig. 5 The photocatalytic mechanism diagram of the urea-treated Ag_3PO_4/g-C_3N_4 photocathode in this photo-assisted MES.

Fig. 6 Acetate production (A), $CE_{acetate}$ (B), solar-to-acetate efficiency (C), accumulated catalyst leaching (D) and Nyquist plots of EIS (E) over 12 days continued operation with periodical addition of bicarbonate for different photocathodes. Ag 3d high resolution XPS spectra of the urea-treated Ag_3PO_4/g-C_3N_4 cathodes after 12 days operation (F).

Figure 1

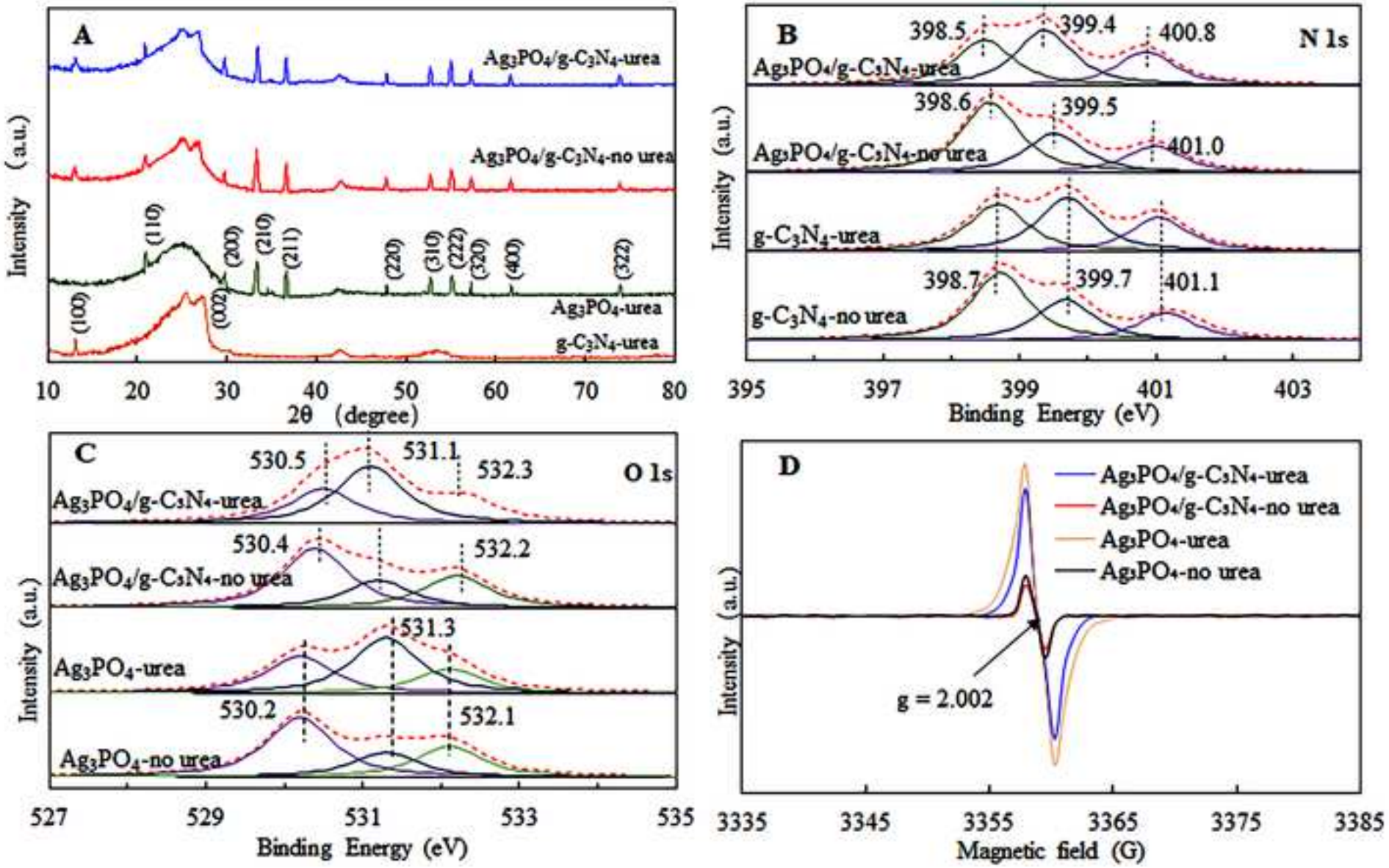
A
Ag3PO4/g-C3N4-urea
Ag3PO4/g-C3N4-no urea
Ag3PO4-urea
g-C3N4-urea
(100)
(002)
(110)
(200)
(210)
(211)
(220)
(310)
(222)
(320)
(400)
(322)
Intensity (a.u.)
2θ (degree)
B
N 1s
398.5
399.4
400.8
398.6
399.5
401.0
398.7
399.7
401.1
Binding Energy (eV)
C
O 1s
530.5
531.1
532.3
530.4
532.2
531.3
530.2
532.1
Binding Energy (eV)
D
g = 2.002
Magnetic field (G)

Figure 2

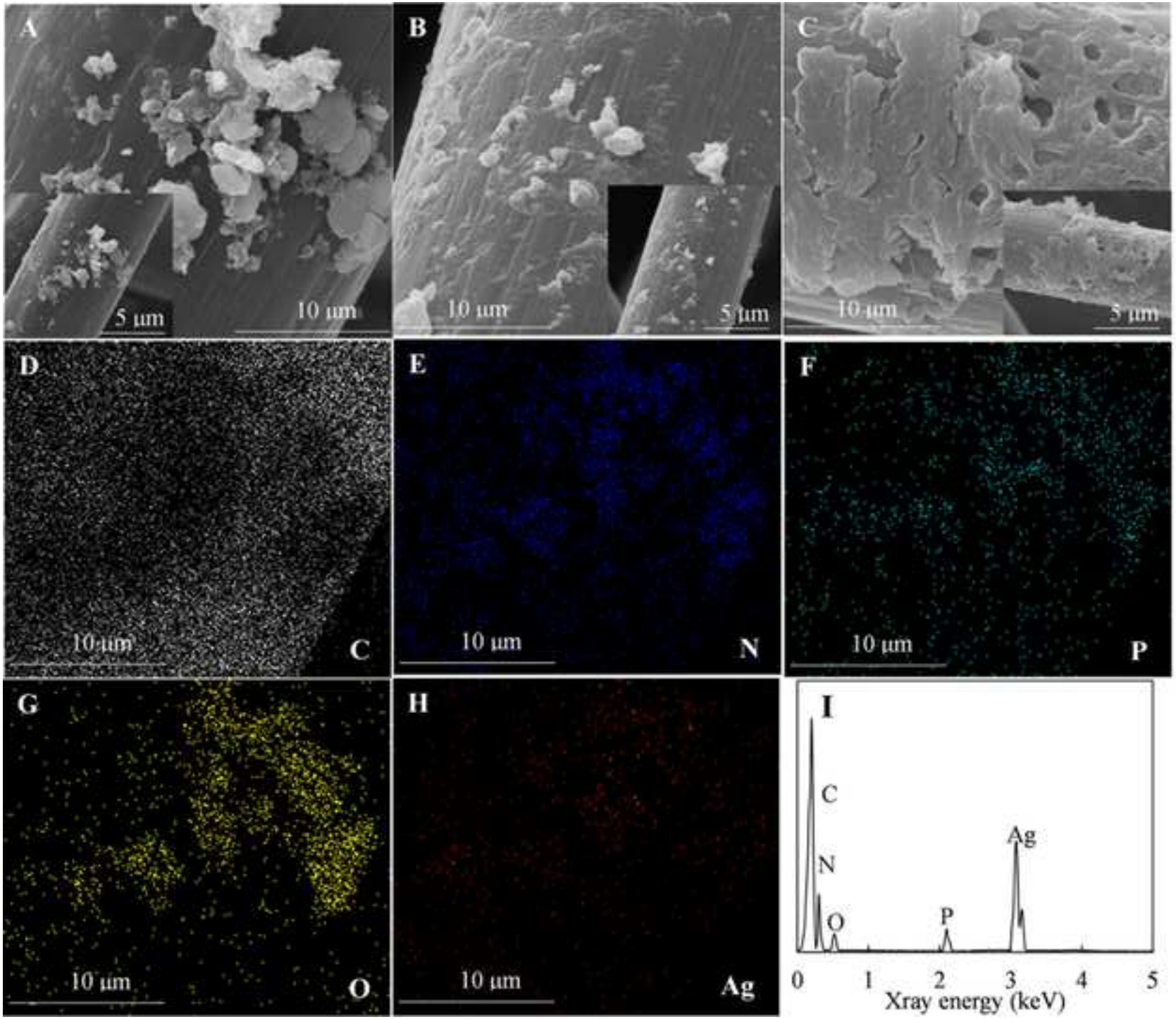
A
5 μm
10 μm
B
10 μm
5 μm
C
10 μm
5 μm
D
10 μm
C
E
10 μm
N
F
10 μm
P
G
10 μm
O
H
10 μm
Ag
I
C
N
O
P
Ag
0
1
2
3
4
5
Xray energy (keV)

Figure 3

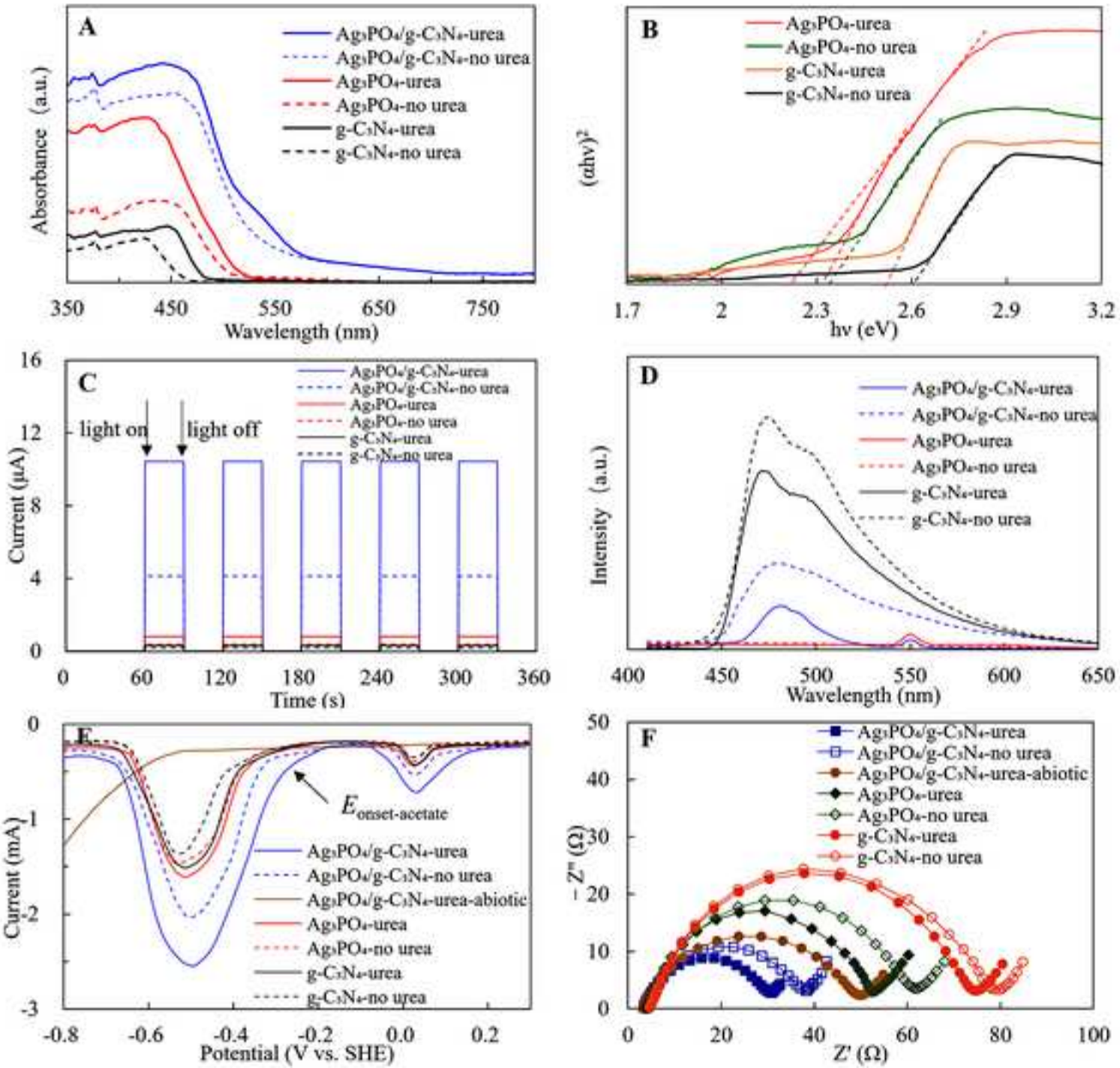
A
Ag3PO4/g-C3N4-urea
Ag3PO4/g-C3N4-no urea
Ag3PO4-urea
Ag3PO4-no urea
g-C3N4-urea
g-C3N4-no urea
Absorbance (a.u.)
Wavelength (nm)
B
Ag3PO4-urea
Ag3PO4-no urea
g-C3N4-urea
g-C3N4-no urea
(αhν)²
hν (eV)
C
light on
light off
Current (μA)
Time (s)
D
Intensity (a.u.)
Wavelength (nm)
E
Eonset-acetate
Ag3PO4/g-C3N4-urea-abiotic
Current (mA)
Potential (V vs. SHE)
F
Ag3PO4/g-C3N4-urea-abiotic
- Z'' (Ω)
Z' (Ω)

Figure 4

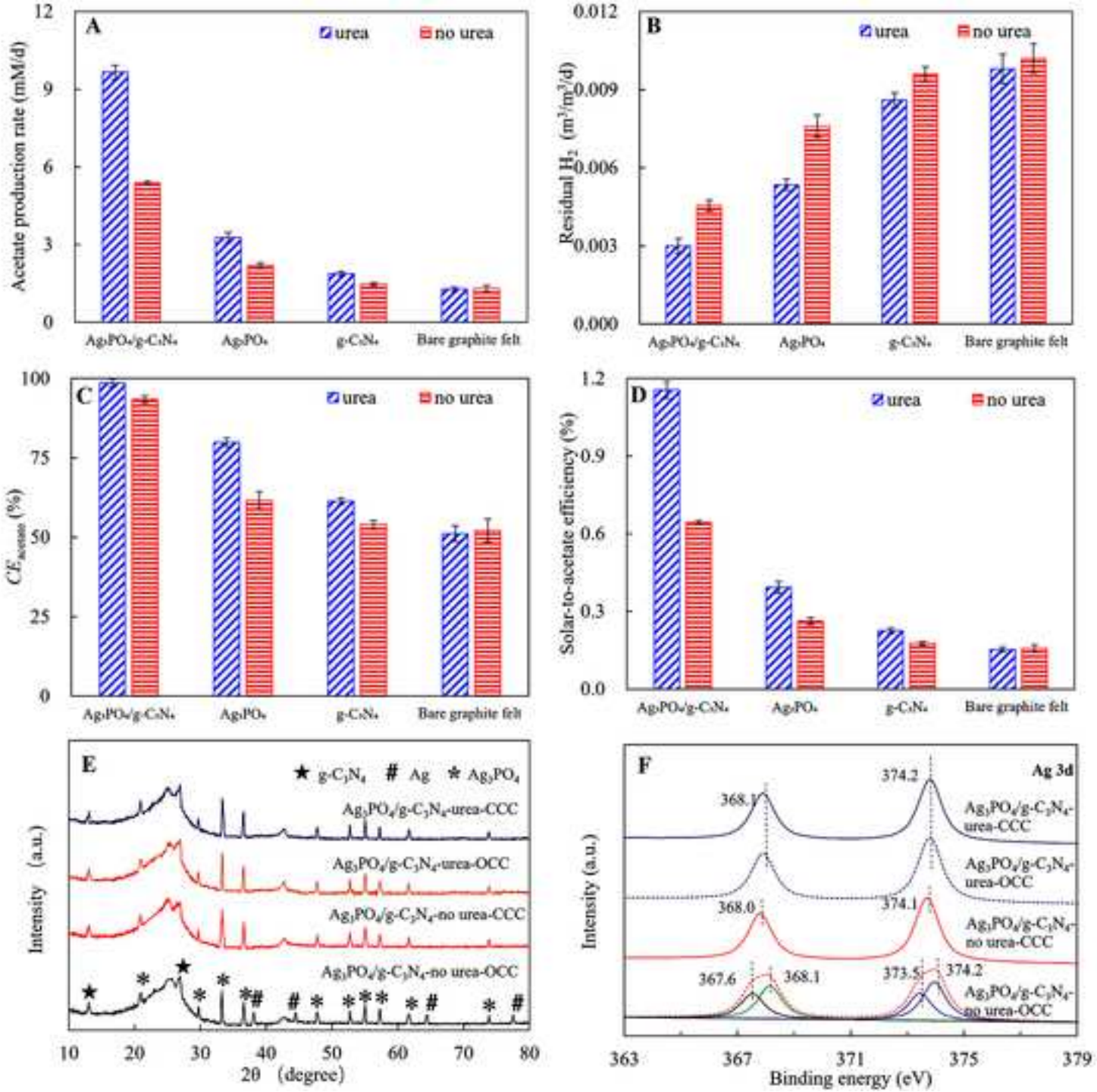
A
urea
no urea
Acetate production rate (mM/d)
Ag3PO4/g-C3N4
Ag3PO4
g-C3N4
Bare graphite felt
B
Residual H2 (m3/m3/d)
C
CE acetate (%)
D
Solar-to-acetate efficiency (%)
E
★ g-C3N4 # Ag ✲ Ag3PO4
Ag3PO4/g-C3N4-urea-CCC
Ag3PO4/g-C3N4-urea-OCC
Ag3PO4/g-C3N4-no urea-CCC
Ag3PO4/g-C3N4-no urea-OCC
Intensity (a.u.)
2θ (degree)
F
Ag 3d
374.2
368.1
374.1
368.0
367.6
373.5
Binding energy (eV)

Figure 5

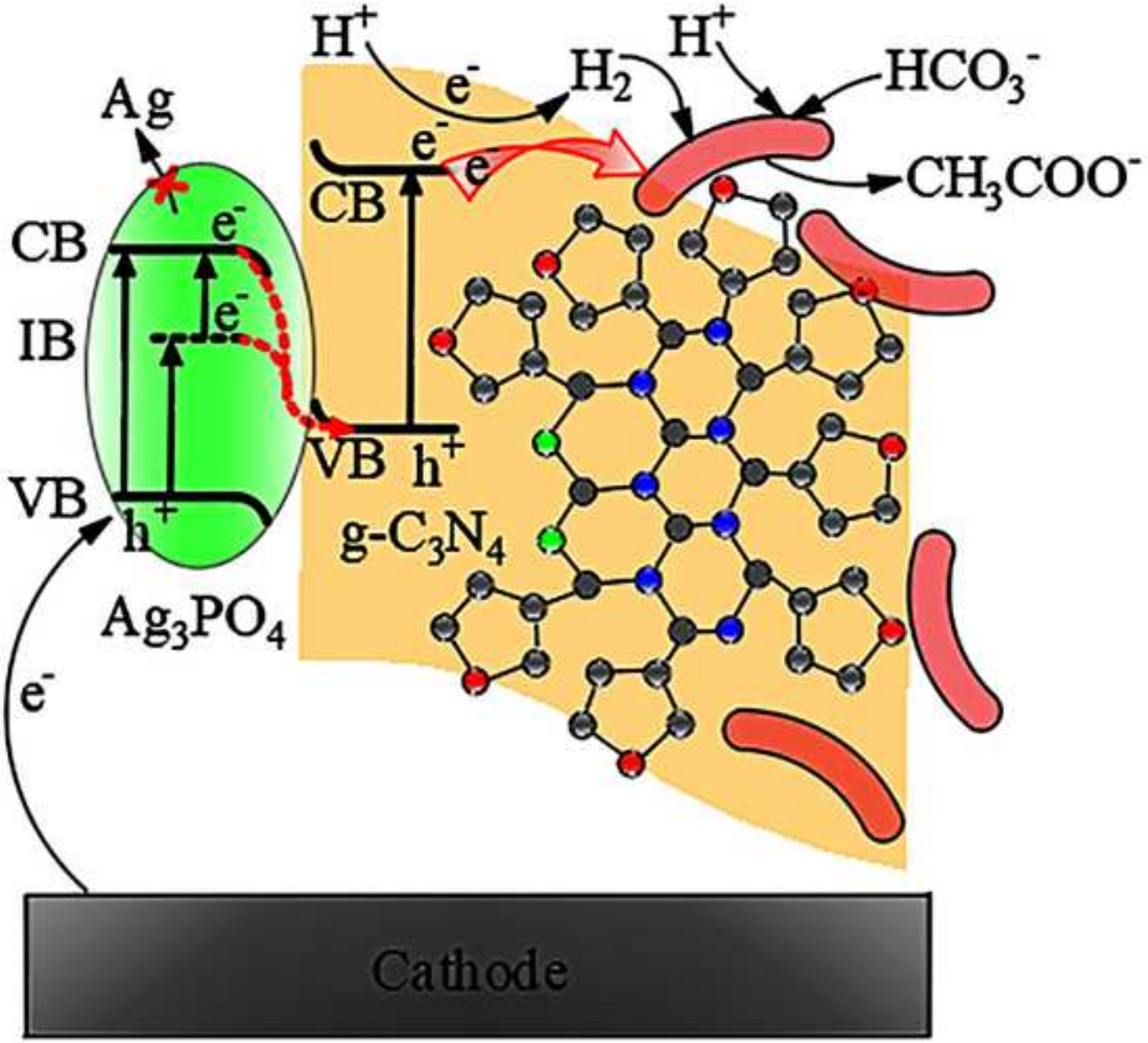
H+
e-
H2
H+
HCO3-
Ag
e-
e
CB
CH3COO-
e-
CB
e-
IB
VB h+
VB
h+
g-C3N4
Ag3PO4
e-
Cathode

Figure 6

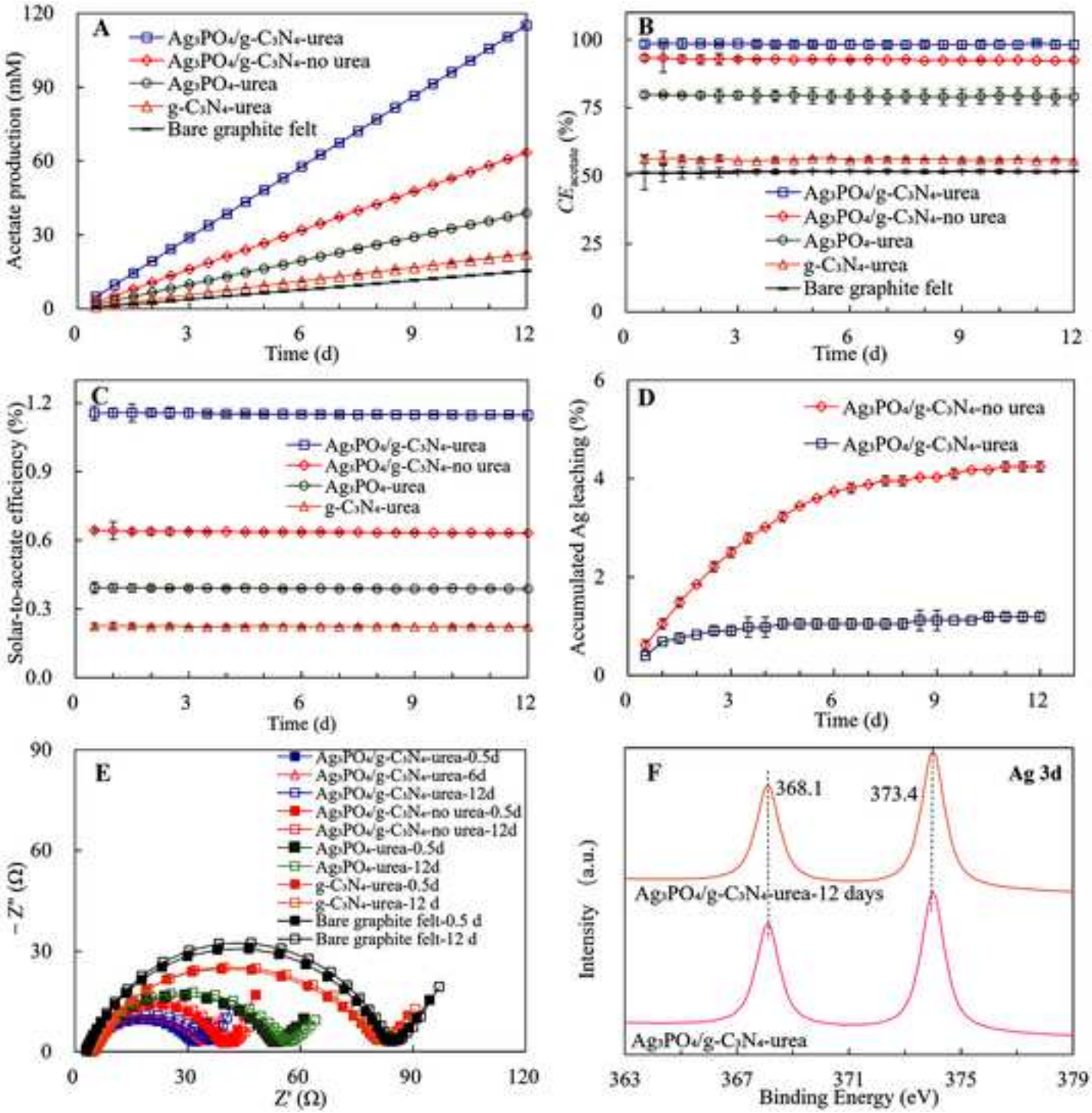
A
Ag3PO4/g-C3N4-urea
Ag3PO4/g-C3N4-no urea
Ag3PO4-urea
g-C3N4-urea
Bare graphite felt
Acetate production (mM)
Time (d)
B
CE acetate (%)
Time (d)
C
Solar-to-acetate efficiency (%)
Time (d)
D
Ag3PO4/g-C3N4-no urea
Ag3PO4/g-C3N4-urea
Accumulated Ag leaching (%)
Time (d)
E
Ag3PO4/g-C3N4-urea-0.5d
Ag3PO4/g-C3N4-urea-6d
Ag3PO4/g-C3N4-urea-12d
Ag3PO4/g-C3N4-no urea-0.5d
Ag3PO4/g-C3N4-no urea-12d
Ag3PO4-urea-0.5d
Ag3PO4-urea-12d
g-C3N4-urea-0.5d
g-C3N4-urea-12 d
Bare graphite felt-0.5 d
Bare graphite felt-12 d
- Z'' (Ω)
Z' (Ω)
F
Ag 3d
368.1
373.4
Ag3PO4/g-C3N4-urea-12 days
Ag3PO4/g-C3N4-urea
Intensity (a.u.)
Binding Energy (eV)